Tuning Quantum-Dot Organization in Liquid Crystals for Robust Photonic Applications

Andrea L. Rodarte,[a] Zachary S. Nuno,[a] Blessing H. Cao,[b] Ronald J. Pandolfi,[a] Makiko T. Quint,[a] Sayantani Ghosh,[a] Jason E. Hein,[b] and Linda S. Hirst*[a]

Mesogenic ligands have the potential to provide control over the dispersion and stabilization of nanoparticles in liquid crystal (LC) phases. The creation of such hybrid materials is an important goal for the creation of soft tunable photonic devices, such as the LC laser. Herein, we present a comparison of isotropic and mesogenic ligands attached to the surface of CdSe (core-only) and CdSe/ZnS (core/shell) quantum dots (QDs). The mesogenic ligand's flexible arm structure enhances ligand alignment, with the local LC director promoting QD dispersion in the isotropic and nematic phases. To characterize QD disper-sion on different length scales, we apply fluorescence micros-copy, X-ray scattering, and scanning confocal photolumines-cent imaging. These combined techniques demonstrate that the LC-modified QDs do not aggregate into the dense clusters observed for dots with simple isotropic ligands when dispersed in liquid crystal, but loosely associate in a fluid-like droplet with an average interparticle spacing > 10 nm. Embedding the QDs in a cholesteric cavity, we observe comparable coupling effects to those reported for more closely packed isotropic ligands.

1. Introduction

Semiconductor nanoparticles (quantum dots, QDs) have gener-ated significant interest because of their unique size-tunable properties arising from quantum confinement effects. Such particles have been shown to be useful as building blocks for a wide variety of applications, such as in optoelectronic devi-ces, drug-delivery systems, and biochemical sensors.[1–5] Recent-ly, significant work has been carried out on developing hybrid liquid crystal (LC)/nanoparticle materials. Studies have looked at creating stable dispersions of metallic, magnetic, and semi-conductor particles in the nematic,[6,7] smectic,[8,9] and colum-nar[10,11] thermotropic phases.[12] Different nanoparticles have been shown to readily localize in regions of low order in the LC phases and to stabilize the defect-rich blue phases[13] and the twist grain boundary phase[14] over a wide temperature range.

One of the key challenges in designing nanoparticle/LC hybrid systems for photonic applications is their stabilization as a composite material over long time periods. Nanoparticles exhibit properties not seen in their bulk phase, and bare nano-crystals (not surface-functionalized) are strongly attracted to each other by electromagnetic forces, producing effectively permanent particle aggregates and complete separation from the solvent. Nanoparticles incorporating surface ligands can avoid this fate if there is an entropic cost to close particle-par-ticle approach. By considering the thermodynamics of the LC/ nanoparticle system, surface ligands can be carefully designed to act as a surfactant between particle and solvent. In general, the surface ligands on a particle will define the alignment of the surrounding LC molecules. In the case of large particles (greater than 1 μm in diameter), this interaction is analogous to the surface-anchoring conditions of an LC device. For exam-ple, simple single-chain ligands, such as octadecylamine (ODA), coating a large particle surface will induce homeotropic LC alignment for typical calamitic materials and therefore a radial distribution of LC molecules at the particle surface, producing a defect around the particle in the nematic phase.[15,16] The in-clusion of microscale particles in the nematic phase has been explored extensively in recent years. For large colloidal parti-cles (< ~500 nm in diameter), different topological defects have been shown to form and can be imaged optically[17–19] and even manipulated using the focused light beam of an op-tical trap.[20] Such work relies primarily on optical imaging and although recently smaller colloids (~100–500 nm diameter)[21] have been examined, detailed characterization of particles less than 50 nm in liquid crystal solvents is still a challenge and must be deduced by more indirect means. For example, NMR[22] was recently used to provide information on local in-teractions between liquid crystal molecules and surface ligands.

For large particles, elastic deformation of the host LC phase dominates the physical behavior, but in the case of small nano-particles approaching the length scale of LC molecules, bulk elasticity descriptions must give way to consideration of dis-crete interactions between the surface ligands and the LC mol-

[a] A. L. Rodarte, Z. S. Nuno, R. J. Pandolfi, M. T. Quint, Prof. S. Ghosh, Prof. L. S. Hirst
Department of Physics, School of Natural Sciences
University of California, Merced
5200 Lake Rd, Merced, CA 95343 (USA)
E-mail: lhirst@ucmerced.edu

[b] B. H. Cao, Prof. J. E. Hein
Department of Chemistry and Biochemistry
School of Natural Sciences, University of California, Merced
5200 Lake Rd, Merced, CA 95343 (USA)

These are not the final page numbers! ↗↗

ecules. Entropic forces, excluded volume effects, and local-order parameter perturbations become important in understanding the phase behavior of the system.[23]

The free-energy cost of adding nanoparticles to an LC phase typically promotes either particle clustering, in which particles are depleted from a local area into a small aggregate, or total phase separation. The particles are recruited to regions of low order in the case of existing defects, and across the isotropic-to-nematic phase transition, particles preferentially locate in the disordered isotropic phase, leading to pattern formation.[15, 16, 23]

A lack of control over nanoparticle aggregation in LC materials has hampered fundamental research efforts to produce composites with a well-defined structure. Possible material outcomes range from well-separated "colloidal" dispersions of isolated particles to dispersions that include ordered nanoparticle clusters. Even at relatively low particle concentrations (less than 1 wt %), nanoparticles readily aggregate into large flocs and precipitate out of the LC over a period of hours, unless their surface properties are carefully designed.

To address this problem, there have been recent attempts to design nanoparticles with mesogenic liquid-crystal-like ligands using gold[24–26] and semiconductor[27] nanocrystals. These strategies have proved effective in modulating nanoparticle dispersal in the nematic phase. In general, it has been shown that a rodlike mesogenic segment built into the ligand can align with the surrounding phase, decreasing the free-energy cost of inserting a single nanoparticle when compared to non-mesogenic ligands, such as ODA.

Designing surface-modified QDs for colloidal dispersal or controlled cluster assembly in LC phases is an important goal in the development of soft switchable *meta*-materials for photonic applications. Recently, our group has investigated ODA–QDs as emitters in a cholesteric cavity.[28,30] These nanoparticles tend to form reversible microsized clusters when dispersed in the LC solvent.[16] A finer control of QD assembly either by complete dispersal or controllable cluster packing will greatly enhance the possibilities of these materials for fluid based self-assembling *meta*-materials.

In this Article we describe the synthesis of new QDs functionalized with a mesogenic ligand (LC–QDs). We use both core-only (CdSe) and core/shell (CdSe/ZnS) dots, characterizing their dispersion in the nematic and cholesteric phases after ligand exchange. A flexible ligand arm is designed to allow the rodlike mesogenic segment to align with the surrounding LC molecules in the nematic phase, minimizing local deformation of the LC director. Polarized and fluorescence microscopy studies show that the addition of mesogenic ligands prevents particle clustering in the nematic phase at low concentrations when compared to ODA–QDs. At higher concentrations, QD-rich clusters form, and by using a combination of X-ray diffraction and photoluminescence (PL) imaging we demonstrate that LC–QD cluster packing in the nematic phase is significantly different to that seen for ODA–QDs. Combining different techniques in a multiscale approach allows us to completely characterize the hybrid material, probing particle packing and interactions for different LC/QD combinations.

2. Results and Discussion

2.1. Quantum-Dot Synthesis and Characterization

To investigate the effects of mesogenic ligands on QD dispersion and the photonic properties of QD/LC hybrid materials, we prepared four different particles, core only and core–shell QDs with either mesogenic (LC–QDs) or ODA ligands (ODA–QDs), as depicted in Figure 1. The ODA ligand has been previ-
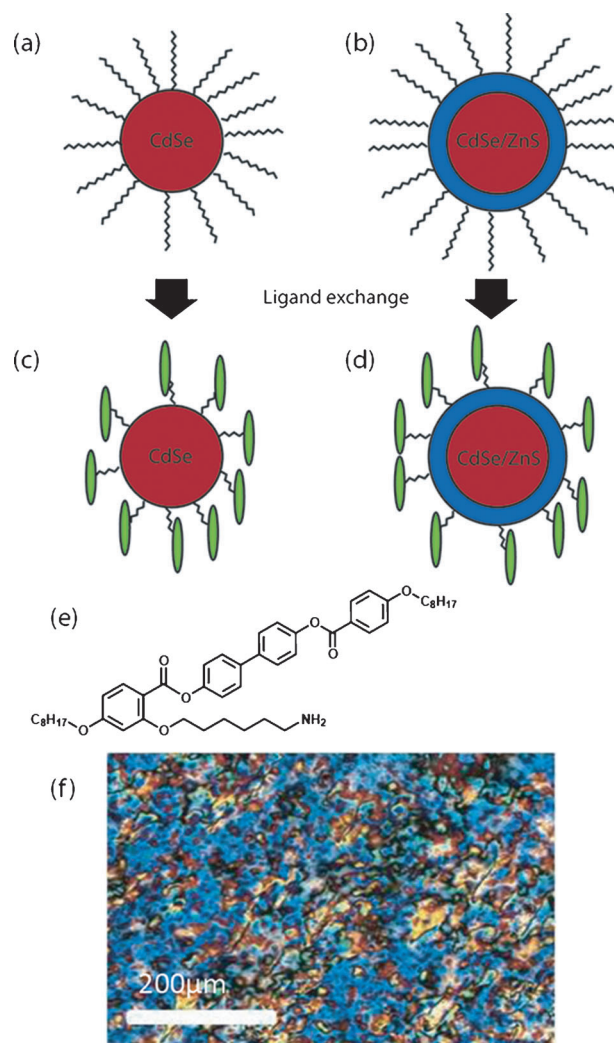

Figure 1. Schematic representation of a–d) the different quantum dots used in this study including non-mesogenic ODA ligands and the LC ligand (green). e) Molecular structure of the mesogenic ligand (11) and f) nematic phase of 11 at 130 °C, imaged by using polarized optical microscopy.

ously shown to promote nanoparticle clustering on both gold and semiconductor particles,[16] whereas mesogenic ligands attached to gold particles have been recently demonstrated to promote more uniform dispersion in the nematic phase. Recently, dendrimer-like ligands were also successfully designed to optimize QD dispersion in a liquid crystal.[27]

ODA-functionalized QDs were supplied by NNlabs Inc. The mesogenic ligand (11) was synthesized as shown in Scheme 1

A)

B)

C)
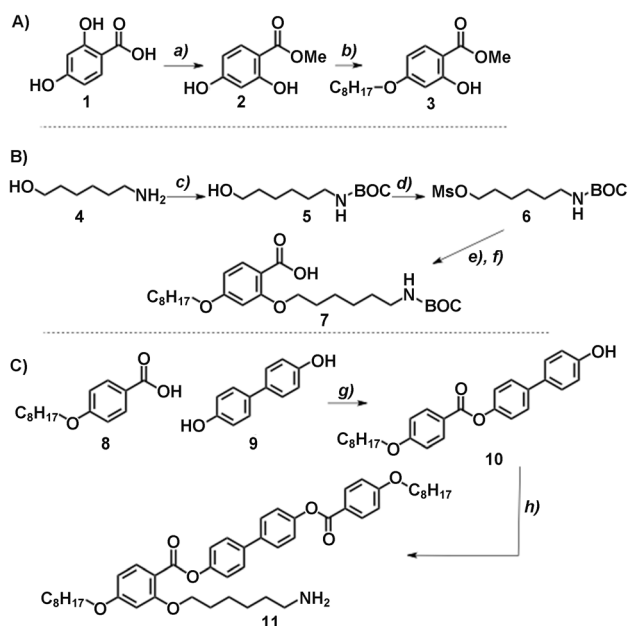
Scheme 1. Synthesis of the liquid-crystal ligand: a) H₂SO₄, MeOH; b) 1-bromooctane, K₂CO₃, 2-butanone; c) (BOC)₂O, DCM; d) MsCl, TEA, DCM; e) KOtBu, KI, 2-butanone; f) NaOH, MeOH; g) DMAP, EDCI, TEA, THF; h) SOCl₂, toluene

and detailed in the Experimental Section. Compound **11** (Figure 1e) is liquid crystalline, forming a nematic phase in its pure state. A liquid-crystal texture for this phase is shown in Figure 1f. The rigid core of compound **11** consists of a typical mesogenic unit, while the flexible arm segment allows rotation of the core once attached to a particle surface. Starting with ODA–QDs, a ligand exchange was performed on both core-only and core/shell QDs to replace ODA with compound **11**.

Figure 2 shows absorption and emission spectra for each of the four particle types, that is, before and after the ligand exchange. Comparing data before and after the exchange process highlights some important differences between the core-only and core/shell semiconductor particles. These plots reveal that the core-only QDs exhibit a significant blue shift in both the absorption and emission spectra after attachment of the new ligand (Figure 2a,b). In contrast, the core/shell particle spectra are almost unchanged after the ligand exchange. QDs prepared without a shell are highly susceptible to oxidation of the core, and this leads to an effective reduction of the QD size. Since the spectral properties of QDs

depend on the particle size, a blue shift in absorption and emission can be attributed to core oxidation. In addition to this blue shift, we also observed that the core-only QDs' emission intensity was significantly reduced after the exchange. This effect may be due to oxidation-induced surface-defect states that trap electrons, quenching PL emission. For these reasons, core/shell QDs should be preferred for photonic applications where stability and quantum efficiency are important performance factors. The use of a protective ZnS shell does increase the overall particle size; however, the additional bulky ligands will increase the minimum obtainable QD separation, a possible factor in applications.

2.2. Quantum-Dot Organization in the Isotropic and Nematic Phases

The goal of this investigation was to characterize the differences between LC–QDs and ODA–QDs when dispersed in nematic and cholesteric liquid crystals with a view towards their use in photonic applications. Therefore, we began by looking at the structure of particle dispersions in the isotropic and nematic phases of the nematic liquid crystal (4-cyano-4'-pentylbiphenyl, 5CB). Using a suite of techniques we cannot only probe QD organization on the microscale, but also characterize particle separation and spectral characteristics on the nanoscale.

Our particles are dispersed in an anisotropic fluid, and so the structure of the composite material is expected to depend on the surface properties of the particle and the liquid-crystalline properties of the host phase. Here, we compare two different cases of surface anchoring, homeotropic alignment using ODA–QDs and LC anchoring using LC–QDs. In the latter case,
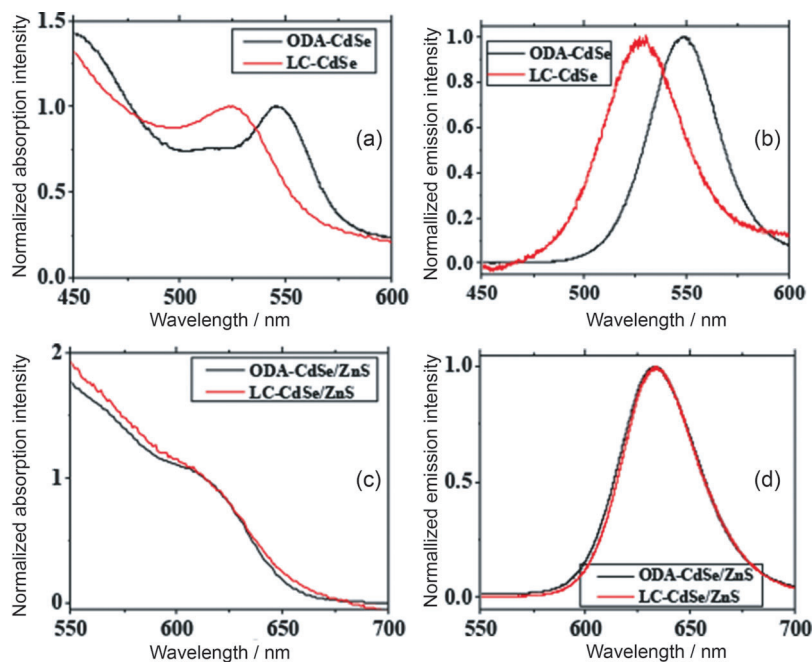

Figure 2. Absorption (a, c) and emission (b, d) spectra for ODA- and LC–QDs in toluene with core-only (a and b) and core/shell (c and d) QDs. Each graph shows spectra taken before and after the ligand exchange.
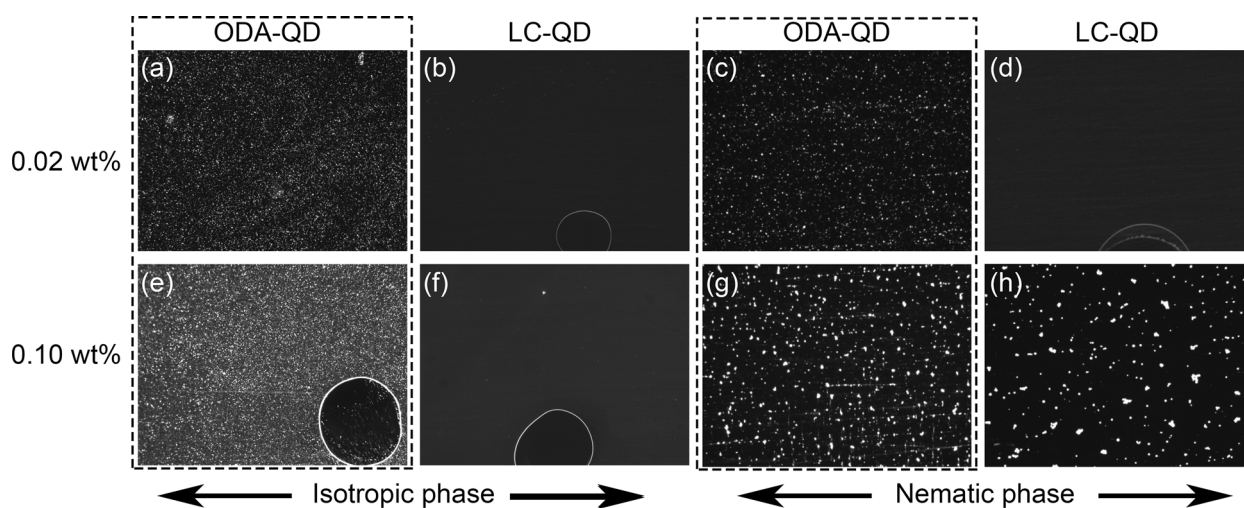
These are not the final page numbers! ↗↗

Figure 3. Fluorescence microscopy images of different surface-functionalized QDs in the isotropic and nematic LC phase (5CB). a) ODA–QD, 0.02 wt %, isotropic. b) LC–QD, 0.02 wt % isotropic. c) ODA–QD, 0.02 wt %, nematic. d) LC–QD, 0.02 wt %, nematic. e) ODA–QD, 0.10 wt %, isotropic. f) LC–QD, 0.10 wt % isotropic. g) ODA–QD, 0.10 wt %, nematic and h) LC–QD, 0.10 wt %, nematic.

the rodlike molecule (11) attached to the particle surface is expected to locally align with the host LC director.

Mixtures were prepared at different QD concentrations in 5CB and imaged using fluorescence microscopy over a range of different concentrations from 0.02 wt % up to 0.15 wt %. In general we found that none of the particle types prepared dispersed uniformly in either the isotropic or the nematic phase above 0.02 wt %. Clear differences could be seen, however, between the ODA–QD and LC–QD particles, particularly at low concentrations. Figure 3 shows a comparison of mixtures prepared with the core/shell QDs in the isotropic phase at two different concentrations after 6 hrs of sonication at 43 °C. These fluorescence images highlight micron-scale QD spatial organization in each of the mixtures. Figures 3 a,b and 3 e,f demonstrate that in the isotropic phase the LC–QDs show enhanced dispersion at both 0.02 wt % and 0.10 wt % with no large clusters visible under the microscope. We observed that the ODA–QDs were only fully dispersed in the isotropic phase (as can be determined by optical microscopy alone) at concentrations < 0.05 wt % with sonication of up to 18 hrs. In comparison, the LC–QDs dispersed well up to concentrations of 0.15 wt % with a 6 hr sonication time.

When we compare the macroscopic differences between ODA–QDs and LC–QDs in the nematic phase (Figure 3, c,d,g,h) we can immediately see that dispersion is less favorable for the ODA–QDs. At the lower concentration (0.02 wt %), LC–QDs disperse uniformly, but ODA-QDs do not; microsized quantum-dot clusters form throughout the material. We observed that the cluster size is a function of cooling rate (from the isotropic to the nematic phase) and concentration. This is expected, since clusters nucleate as a result of thermal particle motion and subsequent depletion from a local area.

For nanoscale particles dispersed in a liquid crystal, entropic effects arising from discrete interactions between surface ligands and surface-localized LC molecules become increasingly important to the phase behavior.[21] The results shown in Figure 3 support this hypothesis, as we can note that in the

isotropic phase there are still dispersion differences between QDs with different ligands despite the fact that the nematic director is no longer present. These differences can be attributed to local ligand–LC interactions near the particle surface.

Fluorescence imaging cannot provide any information on QD organization within clusters below the resolution of light microscopy; therefore, to investigate the material structure in more detail, we performed scanning confocal PL microscopy on the different mixtures. This technique, applied previously by our group,[29–31] produces PL intensity maps of a 1 μm thick slice combined with emission spectra for each pixel recorded. PL microscopy provides a unique method for characterizing the distribution of fluorescent particles in liquid crystals, as energy-transfer processes, such as Forster resonance energy transfer (FRET), can be detected. In this case, if two particles are close together (< 12 nm), FRET produces an average red shift in the QD peak emission as a function of the particle separation. This information can be used to determine the average particle separation within a cluster.[15]

Figure 4 shows PL intensity maps with the corresponding peak-wavelength maps for four different materials: ODA–QDs and LC–QDs in the nematic phase at both 0.02 and 0.1 wt %. In each of the images shown, we focus on a large microscale QD cluster where present. By mapping the peak emission wavelength across a QD cluster, differences in nanoscale particle packing can be elucidated.

Starting at a low concentrations of QDs, the images in Figures 4 a,e are consistent with the fluorescence microscopy images shown in Figure 3. The ODA–QDs cluster into defined aggregates whereas the LC–QDs do not. Notice that in Figure 4 b, (the peak emission wavelength map corresponding to 4 a), there is a significant red shift inside the cluster compared to isolated particles outside the cluster. This indicates that the QDs inside the cluster are relatively closely packed and consistent with recently reported X-ray scattering and PL data,[15, 31] giving an average QD–QD separation of 8.7 nm. Similar results are also seen at higher concentrations (Figures 4 c,d).

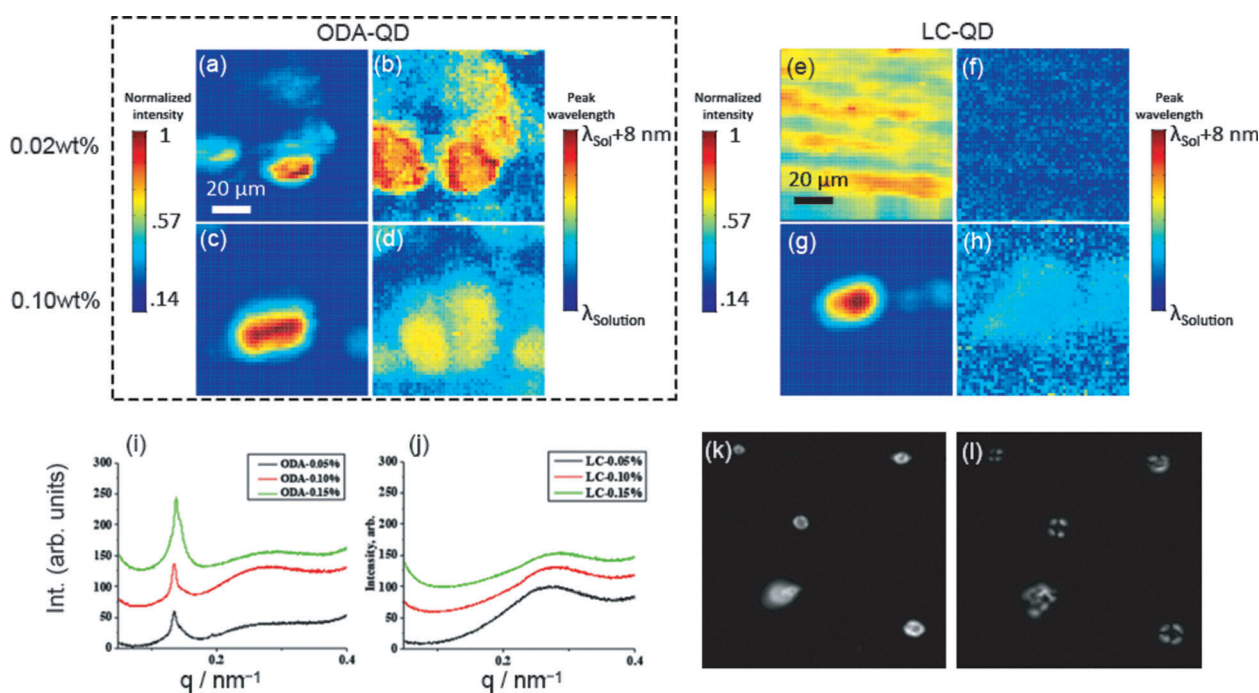These are not the final page numbers! ↗↗

Figure 4. Photoluminescence confocal microscope images of CdSe/ZnS QDs in nematic LC (5CB) are shown for two different concentrations. a) Intensity map and b) peak wavelength map for 0.02 wt% ODA–QD. c) Intensity maps and d) peak wavelength maps for 0.1 wt% ODA–QD. e) Intensity map and f) peak wavelength maps for 0.02 wt% LC–QDs. g) Intensity maps and h) peak wavelength map for 0.1 wt% LC–QDs. Small angle X-ray diffraction data is also shown for i) ODA–QDs at different concentrations in a nematic liquid crystal and j) LC–QD. k) Fluorescence microscopy image of nematic-like LC–QD-rich droplets at 0.1 wt% in 5CB. l) Polarized microscopy image of a similar sample both taken with a 10× objective.

In Figure 3, we see that the LC–QDs show cluster formation at 0.1 wt%. By comparing the PL spectra with those of the ODA–QD clusters, differences become apparent. Figures 4 g,h clearly show that LC–QD clusters exhibit a minimal red-shift. From this result we can conclude that the particles must be ≤ 10 nm apart within the assembly.

Figures 4 i,j show small angle scattering data for the core-only QDA–QDs and LC–QDs, dispersed at 0.05, 0.10, and 0.15 wt% in 5CB. Figure 4 i shows a clear scattering peak at 0.13 nm^{-1} for all three concentrations. In a disordered particle aggregate with a characteristic particle–particle separation, such a peak corresponds to the average distance between neighboring particles.[17] This peak indicates that the particles have a relatively well-defined separation within the aggregates of 4.8 nm. In the case of core QDs with ODA ligands, this indicates a gap of ∼1.7 nm between QDs with some interdigitation of the ODA chains. Carrying out the same measurement on dispersions prepared with the LC–QDs reinforces our conclusions from the PL imaging. The correlation peak is no longer present (Figure 4 j) at any of the concentrations studied. Despite the clear presence of the aggregates visualized using fluorescence microscopy, no X-ray peak was detected after scanning multiple samples and sample regions. This result indicates that the LC–QD aggregates seen with microscopy are more disordered and fluid-like than those observed in the ODA–QD system, with no well-defined inter-dot spacing.

Above 0.05 wt%, close-up fluorescence imaging carried out using a 40× microscope objective reveals that the LC–QD clusters are actually spherical liquid-crystalline droplets and not

the irregular aggregates more characteristic of the ODA–QDs. This can be seen by looking at fluorescence (Figure 4 k) and polarized (Figure 4 l) microscopy images of the same sample area. The LC–QDs form luminescent droplets within the host nematic phase and using a planar alignment for the host phase aligned with one of the polarizers birefringence from the QD-rich structures can be seen with characteristic nematic extinction crosses clearly visible.

These results, when combined with findings from the X-ray measurements and PL spectra provide evidence of fluid–fluid phase separation into a 5CB-rich phase and an LC–QD-rich phase. This result is consistent with observations of LC phase formation in systems of pure LC functionalized nanoparticles[25, 26] and demonstrates how LC ligands much as these can lead to a rich phase behavior. The results described in this section also highlight the importance of carrying out a multiscale characterization of these hybrid materials.

On much larger length scales, QD/LC mixtures have been recently demonstrated to produce interesting patterns, as the materials are slowly cooled from the isotropic to the nematic phase.[16, 23] Particles dispersed in the isotropic phase will seek regions of low order at the phase transition, clustering at defect points. Figure 5 shows an example of this phenomenon for the ODA- and LC–QDs. Figures 5 a–c show fluorescence and PL images of ODA–QD clusters in the nematic phase. The PL maps of intensity and peak wavelength reveal that these clusters are relatively densely packed with an average QD spacing of 8.7 nm within the cluster as characterized by their FRET red shift. In comparison, imaging the LC–QDs as the mixture is
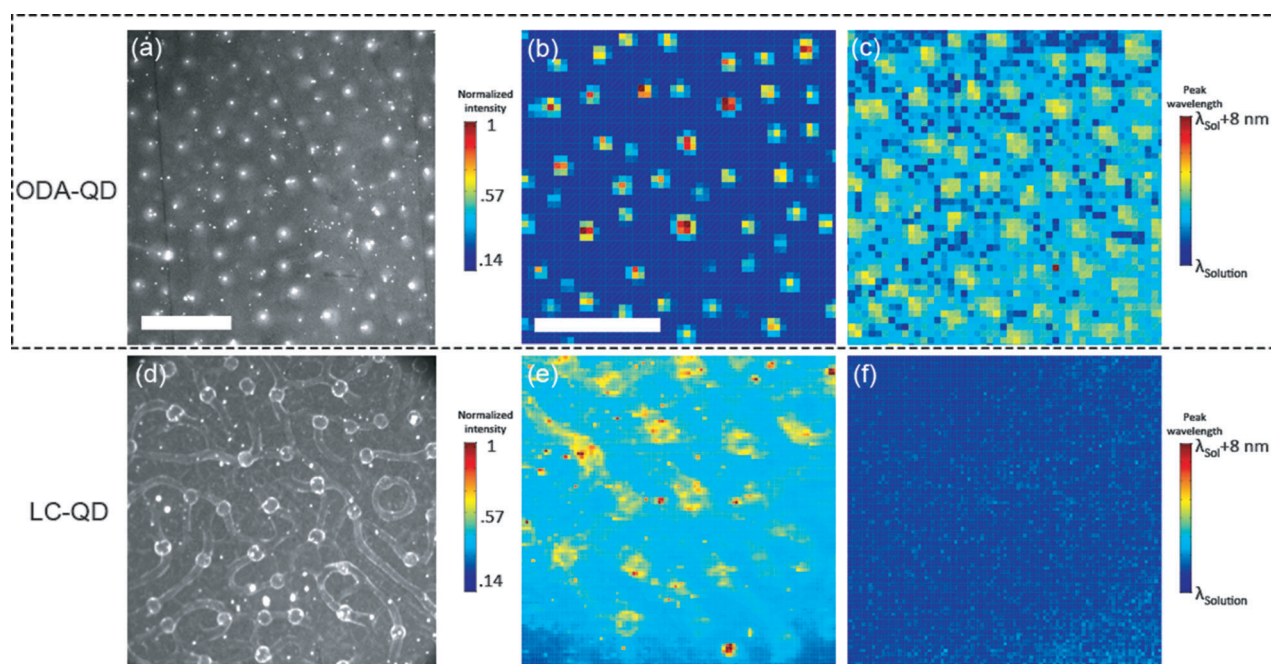
These are not the final page numbers! ⤢⤢

Figure 5. Images characterizing large-scale pattern formation in nematic/QD mixtures comparing the ODA and LC ligands. Fluorescence microscopy (a,d), photoluminesence intensity (b,e), and peak emission wavelength (c,f) for ODA–QD and LC–QDs at 0.1 wt % in 5CB are shown (scale bars = 200 μm).

cooled slowly (Figures 5 d–f) reveals some bright clusters with an additional diffuse wormlike pattern. The diffuse pattern forms as the QDs move into the remaining isotropic regions as the material is cooled to the nematic phase. Similar patterns for ODA–QDs have also been observed on very slow cooling.[15] The PL images for this mixture (Figures 5 e,f) show that neither the brightest clusters or the diffuse pattern exhibit any significant red shift, demonstrating that the LC–QDs are at least 12 nm apart across the sample. Analysis of such pattern formation using a combination of fluorescence and PL imaging should provide an interesting probe into the thermodynamics of these systems and will be the subject of future investigations.

2.3. Performance in Soft Photonic Devices

The ability to stably disperse QDs in a liquid-crystal host material provides us with the possibility of soft-assembling photonic devices. In cholesteric devices, embedded QDs can act as emitters coupled to a tunable fluid cavity, producing applications such as the quantum dot liquid crystal laser[32] and switchable cavities able to spatially modulate QD emission.[29,31] The efficiency of such devices will depend on our control of co-operative effects between adjacent particles. For example energy transfer processes such as FRET can reduce the efficiency of QD cavity coupling if the particles are closely packed in aggregates. Therefore by designing appropriate QD ligands, particle clustering and dispersion can be tuned to optimize device performance.

Figure 6 shows a comparison of the ODA–QD and LC–QD emissions in a cholesteric cavity. The plots include the emission spectra (separated into left and right circular polarizations) of
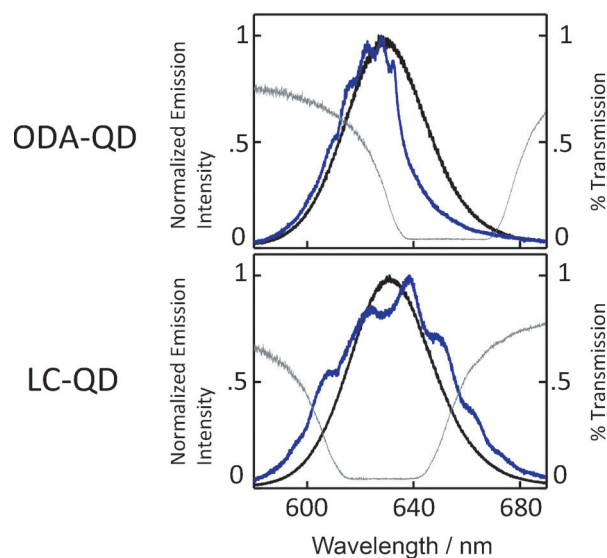

Figure 6. Emission spectra for ODA- and LC–QDs dispersed in a cholesteric material (see Experimental Section) at 0.1 wt % and separated into left-handed (black peak) and right-handed (blue peak) components. The cholesteric stop band (transmission spectrum) is also shown (grey) for the right-handed component.

the embedded QDs and the cholesteric stop band. The QD emission spectra reveal clear resonances with the cholesteric cavity for the right-handed component only, as expected. Heating to the isotropic phase removes the resonant structure and the blue (right handed) curve becomes smooth (results not shown). Higher power densities should lead to lasing in a high quality cavity, but in this system lasing was not observed at any applied power. This result may be due to a reduc-

tion in cavity quality caused by the large QD-rich aggregates in the system. A large number of Grandjean defects where seen for these materials. In addition, a low concentration over-all of emitters when compared with LC/dye lasers is used. These results however demonstrate that the LC ligands do not adversely impact cavity resonance effects. Therefore, by modi-fying the mesogenic ligand design to produce a uniform QD dispersion at high concentrations it may be possible to induce lasing in these materials.

3. Conclusion

LC/QD hybrid materials can be potentially applied to new pho-tonic device technologies. Before such ideas can be realized, a clear understanding of particle organization within the host material should be established. Elastic deformations of the nematic director play an important role in phase-separation phenomena and can lead to clustering, aggregation, and even disruption of the host liquid-crystal phase. In addition, at very small length scales, entropic effects can contribute significantly and should be taken into account. We have designed and syn-thesized a new QD incorporating a mesogenic ligand on a flexi-ble arm capable of aligning with local nematic ordering. We report that core/shell QDs incorporating the LC ligand show excellent dispersion in the isotropic phase and reduced clustering in the nematic phase, with a good dispersion at low concentrations and stable optical performance on ligand at-tachment. Looking deeper into the structure of the QD clusters for the different ligands, scanning confocal PL microscopy and small angle X-ray diffraction reveal that the LC–QD clusters ob-served at concentrations above 0.05 wt% are phase-separated liquid-crystalline domains, rich in LC–QDs with an inter-particle separation > 12 nm. In a cholesteric device, the new LC–QDs perform comparably to the ODA–QDs but may find use in ap-plications that take advantage of their fluidlike structure for tunable QD assembly.

Experimental Section

General Method

The LC ligands were synthesized according to Scheme 1. *p*-Alkyat-ed phenol **3** was first generated via esterification of **2** followed by Williamson etherification selectively at the 4-position. The *ortho*-functionality was then added via coupling with N-Boc mesylate **6**, which was synthesized by *N*-protection followed by *O*-mesylation. The LC-ligand core was obtained by esterification with acid **8** and bis-phenol **9** to give alcohol **10**, which was finally coupled to acid **7** via in situ acid chloride generation. This final coupling both acti-vated the carboxylic acid group and removed the *N*-Boc protection to yield the final ligand **11**.

Synthesis of Methyl 2,4-Dihydroxybenzoate (2)

2,4-dihydroxybenzoic acid **1** (12 g, 78 mmol) was added to MeOH (60 mL) and stirred. Concentrated sulfuric acid (5 mL, 94 mmol) was then added dropwise. The whole mixture was heated to reflux overnight. MeOH was removed under vacuum and the residue was poured into 200 mL ice water. Methyl 2,4-dihydroxybenzoate 2

(12.8 g, 98% yield) was isolated using a filter. The characterization data matched that of a previous report.[33]

Synthesis of Methyl 2-Hydroxy-4-(Octyloxy)benzoate (3)

Methyl 2,4-dihydroxybenzoate **2** (7.8 g, 46.4 mmol) was dissolved in butanone (155 mL) and treated with 10 g of molecular sieves (4A) and potassium carbonate (32.1 g, 232 mmol). The whole reac-tion was heated to reflux. A solution of 1-bromooctane (9.85 g, 51.0 mmol) in butanone (30.9 mL) was added into the refluxing re-action at a rate of 0.5 mL min^{-1}, and then the vessel was heated for an additional 18 hrs. The reaction was filtered, and the solvent was removed under vacuum. Methyl 2-hydroxy-4-(octyloxy)ben-zoate **3** (12.29 g, 94% yield) was the isolated by re-recrystallization from MeOH. ^{1}H NMR (400 MHz, CDCl$_3$) $\delta = 10.92$ (s, 1 H), 7.69 (d, $J = 9.5$ Hz, 1 H), 6.40 (s, 1 H), 6.40–6.36 (m, 1 H), 3.93 (t, $J = 6.4$ Hz 2 H), 3.87 (s, 3 H), 1.74 (dq, $J = 8.4$, 6.6 Hz, 2 H), 1.48–1.19 (m, 10 H), 0.85 ppm (t, $J = 6.6$ Hz, 3 H); ^{13}C NMR (101 MHz, CDCl$_3$) $\delta = 170.37$, 165.17, 163.69, 131.08, 107.90, 105.14, 101.07, 68.24, 51.87, 31.74, 29.25, 29.16, 28.95, 25.91, 22.60, 14.04 ppm.

Synthesis of Tert-butyl (6-hydroxyhexyl)carbamate (5)

A solution of 6-aminohexan-1-ol **4** (10 g, 85 mmol) in DCM (53 mL) was treated with a solution of di-tert-butyl dicarbonate (20.11 g, 92 mmol) in DCM (53 mL) added at a rate of 1 mL min^{-1} The reac-tion was stirred at room temperature overnight. Solvent was re-moved under vacuum. The residue was diluted with diethyl ether, extracted with dilute acetic acid, and then washed once with NaHCO$_3$ solution and dried with Na$_2$SO$_4$. The organic layer was re-moved under vacuum and yielded (16.7 g, 84% yield) of tert-butyl (6-hydroxyhexyl)carbamate **5**. The characterization data matched that of a previous report.[34]

Synthesis of 6-((Tert-butoxycarbonyl)amino)hexyl Methane-sulfonate (6)

Tert-butyl (6-hydroxyhexyl)carbamate **5** (10 g, 47 mmol) was dis-solved in DCM (235 mL). Triethylamine (8.51 mL, 61.1 mmol) was added and the mixture was cooled down to 0°C. Methansulfonyl chloride (4.39 mL, 56.4 mmol) was then added dropwise. The reac-tion was stirred for four hours and then quenched with water (235 mL). The reaction was extracted three times with DCM, dried with Na$_2$SO$_4$. The solvent was removed under vacuum to yield 6-((tert-butoxycarbonyl)amino)hexyl methanesulfonate **6** (13.6 g, 98% yield). ^{1}H NMR (400 MHz, CDCl$_3$) $\delta = 4.18$ (t, 2 H, $J = 6.4$ Hz), 3.06 (t, 2 H, $J = 6.6$ Hz), 2.96 (s, 3 H), 1.72 (tt, 2 H, $J = 7.7$, 6.3 Hz), 1.40 (s, 9 H), 1.48–1.31 ppm (m, 6 H); ^{13}C NMR (101 MHz, CDCl$_3$) $\delta = 155.99$, 79.16, 69.86, 37.34, 29.85, 29.00, 28.37, 26.11, 25.07 ppm.

Synthesis of 2-((6-((Tert-butoxycarbonyl)amino)hexyl)oxy)-4-(octyloxy)benzoic acid (7)

A solution of methyl 2-hydroxy-4-(octyloxy)benzoate **3** (1.2 g, 4.28 mmol) in methy-ethyketone (22.8 mL) was added to a solution of 6-((tert-butoxycarbonyl)amino)hexyl methanesulfonate **6** (1.391 g, 4.71 mmol) in methy-ethyketone (20 mL). Potassium iodide (1.066 g, 6.42 mmol) and potassium tertbutoxide (0.576 g, 5.14 mmol) were added as powders. The reaction was heated to reflux for 24 h. The solvent was removed under vacuum. The resi-due was then dissolved in 100 mL water, and extracted three times with 50 mL of DCM, and dried with Na$_2$SO$_4$. The organic layer was placed under vacuum to yield methyl 2-((6-((tert-butoxycarbonyl)-amino)hexyl)oxy)-4-(octyloxy)benzoate (1.93 g, 94% yield).

These are not the final page numbers! ↗↗

Methyl 2-((6-((tert-butoxycarbonyl)amino)hexyl)oxy)-4-(octyloxy) benzoate (1.933 g, 4.03 mmol)) was dissolved in MeOH (81 mL). Sodium hydroxide (20.15 mL, 40.3 mmol) was added and the reaction was stirred at 55 °C overnight. Solvent was removed under vacuum and acidified with conc. HCl (pH 2–4), then extracted with DCM, and dried with Na_2SO_4. The organic solvent was removed under vacuum. The residue was recrystalized with a minimum volume of hexane to yield 2-((6-((tert-butoxycarbonyl)amino)hexyl)oxy)-4-(octyloxy)benzoic acid **7** (1.19 g, 63% yield). ^{1}H NMR (400 MHz, CDCl$_3$) $\delta = 8.06$ (d, $J = 8.8$ Hz, 1H), 6.58 (dd, $J = 8.8$, 2.2 Hz, 1H), 6.46 (d, $J = 2.2$, Hz, 1H), 4.15 (t, $J = 6.5$ Hz, 2H), 3.97 (t, $J = 6.5$ Hz, 2H), 3.09 (t, $J = 6.9$ Hz, 2H), 2.06–1.83 (m, 2H), 1.76 (dd, $J = 8.3$, 6.4 Hz, 2H), 1.40 (s, 9H), 1.54–1.20 (m, 16H), 0.85 ppm (t, $J = 7.0$, 3H); ^{13}C NMR (101 MHz, CDCl$_3$) $\delta = 165.31$, 164.57, 158.87, 135.35, 107.05, 99.74, 77.29, 76.98, 76.66, 69.92, 68.53, 31.73, 29.90, 29.24, 29.15, 29.00, 28.72, 28.37, 26.27, 25.90, 25.53, 22.59, 14.04 ppm.

Synthesis of 4′-Hydroxy-[1,1′-biphenyl]-4-yl 4-(octyloxy)-benzoate (10)

4-(octyloxy)benzoic acid **8** (2 g, 7.99 mmol), [1,1′-biphenyl]-4,4′-diol **9** (1.488 g, 7.99 mmol), and DMAP (0.195 g, 1.598 mmol) were dissolved in THF (44 mL). The sample was then treated with triethylamine (2.56 mL, 18.38 mmol). Finally, EDCI–HCl (1.84 g, 9.60 mmol; EDCI = 1-ethyl-3-(3-dimethylaminopropyl)carbodiimide) was added, and the reaction was stirred for two days at room temperature to give a milky solution. The sample was filtered and the solids were washed with DCM. The filtrate solvent was removed under vacuum. The residue was treated with EtOH, heated to reflux, and filtered while hot. The clear filtrate was cooled to room temperature to allow a crystal to form, which was then isolated by filtration to yield 4′-hydroxy-[1,1′-biphenyl]-4-yl 4-(octyloxy)benzoate **10** (0.97 g, 29% yield). The characterization data matched that of a previous report.[35]

Synthesis of 4′-((4-(Octyloxy)benzoyl)oxy)-[1,1′-biphenyl]-4-yl 2-((6-aminohexyl)oxy)-4-(octyloxy)benzoate (11)

2-((6-((tert-butoxycarbonyl)amino)hexyl)oxy)-4-(octyloxy)benzoic acid **7** (0.64 g, 1.375 mmol) was dissolved in toluene (7.64 mL). Thionyl chloride (0.181 mL, 2.474 mmol) was added dropwise, and the reaction was stirred at room temperature for 24 h. The conversion to acid chloride was monitored by HPLC. Finally, 4′-hydroxy-[1,1′-biphenyl]-4-yl 4-(octyloxy)benzoate **10** (0.449 g, 1.074 mmol) was added directly into the reaction, which was then heated to 60 °C for 48 h. The solvent was removed under vacuum. The residue was dissolved in MeOH and heated up to 70 °C for one hour. Then, MeOH was removed under vacuum. This process was repeated once more with MeOH, finally giving 4′-((4-(octyloxy)benzoyl)oxy)-[1,1′-biphenyl]-4-yl 2-((6-aminohexyl)oxy)-4-(octyloxy)benzoate **11** (1.15 g, 87% yield) as a white powder. ^{1}H NMR (400 MHz, [D$_8$]Toluene) $\delta = 8.16$–8.06 (m, 2H), 8.07–7.96 (m, 1H), 7.52–7.36 (m, 4H), 7.25–7.12 (m, 4H), 6.74–6.65 (m, 2H), 6.42 (s, 1H), 6.35–6.25 (m, 1H), 3.67 (dd, $J = 15.4$, 8.5 Hz, 4H), 3.55 (t, $J = 6.3$ Hz, 2H), 2.88 (s, 2H), 1.56 (dt, $J = 15.0$, 8.7 Hz, 6H), 1.38–1.07 (m, 26H), 0.95–0.78 ppm (m, 6H). ^{13}C NMR (101 MHz, toluene) $\delta = 164.37$, 164.21, 163.61, 163.31, 161.71, 150.97, 150.62, 137.67, 137.19, 132.17, 127.86, 122.36, 122.09, 121.93, 114.07, 111.48, 67.81, 31.91, 31.86, 31.82, 29.53, 29.43, 29.36, 29.30, 29.27, 29.14, 26.08, 25.98, 22.70, 22.68, 22.66, 13.95, 13.91, 13.88 ppm.

Ligand Exchange

The commercial quantum dots were washed using a precipitation–redispersion scheme. In the process, 1 mL of quantum-dot solution was precipitated with 1 mL of methanol. The mixture was centrifuged for 10 min and the supernatant was discarded. The precipitate was then redissolved in 1 mL of toluene and washed two more times. Afterwards the precipitate was dissolved in 1 mL of chloroform. A solution of the liquid-crystal ligand **11** dissolved in toluene (40 mmol) was added to the quantum-dot solution, heated to 40 °C, and stirred for three hours. The mixture was then taken off heat and left to cool back to room temperature. Ethyl acetate (2 mL) was then added to the ligand-exchanged quantum-dot solution and centrifuged. The precipitate was washed two more times using a 1:1:2 solution of toluene, chloroform, and ethyl acetate. The preciptate was finally resuspended in 1 mL toluene.

Quantum Dot/Liquid Crystal Mixture Preparation

The different quantum dots are first sonicated in toluene in a sealed glass vial for ~10 mins, then added to a nematic (5CB) or cholesteric (5CB (4-cyano-4′-pentylbiphenyl) and COC (cholesteryl oleyl carbonate) liquid crystal at the required wt%. The mixture is heated to the isotropic phase (above 35 °C for 5CB) and bath-sonicated for eight hours in a glass vial with the cap removed. This method allows the toluene to gradually evaporate from the liquid-crystal mixture as the QDs are dispersed. Almost complete toluene removal is verified by measuring the nematic-to-isotropic phase-transition point by using differential scanning calorimetry, as this transition is very sensitive to the presence of small amounts of additional solvent. The composite material can then be transferred to a microscope slide or glass capillary. Materials are kept above the isotropic phase transition and carefully cooled at the desired rate for microscopy or X-ray diffraction experiments.

Microscopy and Spectroscopic Methods

Polarized optical microscopy is carried out on a Leica DM2500P upright microscope in the transmission mode with a 10× or 20× objective and Linkam heating stage. Fluorescence microscopy (reflection) can also be carried out on the same microscope without polarizers. For fluorescence imaging of the QDs with a peak emission at 620 nm, a 515–560 nm band-pass filter with white-light mercury lamp illumination was used. Emission was detected using a 580 nm dichroic mirror and a 590 nm Long pass filter. The samples were mounted on standard glass slides under a cover slip, homeotropic liquid crystal alignment was achieved using a CTAB surface coating. Absorption spectral measurements for particles in toluene were performed using a PerkinElmer UV/Vis spectrophotometer.

Photoluminescent scanning confocal microscopy was performed using a custom-built high-resolution scanning confocal microscopy system, as described previously.[29] The excitation sources are several ultrafast, tunable mode-locked lasers that cover the spectral region 350–1200 nm, a high-power Ti:Sapphire laser (MIRA 900), and two optical parametric oscillators (OPO). The excitation is focused on the sample with a high numerical aperture objective. The spot size is diffraction-limited (~600 nm). Glass slides containing the QD/LC material are mounted on a heating stage (Instec Inc.) on a computer-controlled 3D scanning stage. The emission (PL) is collected by the same objective (100X) used for excitation. A spectrometer coupled to a thermo-electrically cooled CCD camera produces spectral images with 1 µm spatial resolution.

X-ray Diffraction

Measurements were carried out at the Stanford Synchrotron Radiation Lightsource, beamline 4–2. Liquid crystal/QD mixtures were prepared at the beamline and filled into 1 mm quartz capillaries; measurements were taken 30 hrs after preparation. The capillaries were mounted in transmission configuration using a custom chamber. Measurements were taken at 11 keV for 1 s per exposure at three spatially separated points on each capillary with a beam size of 0.3×0.1 mm at the sample. The area detector data was analyzed at the beamline using the custom SasTool software.

[1] N. M. Park, T. S. Kim, S. J. Park, *Appl. Phys. Lett.* **2001**, *78*, 2575–2577.
[2] L. Zhuang, L. Guo, S. Y. Chou, *Appl. Phys. Lett.* **1998**, *72*, 1205.
[3] J. K. Jaiswal, H. Mattoussi, J. M. Mauro, S. M. Simon, *Nat. Biotechnol.* **2002**, *21*, 47–51.
[4] J. M. Costa-Fernández, R. Pereiro, A. Sanz-Medel, *TrAC Trends Anal. Chem.* **2006**, *25*, 207–218.
[5] A. J. Nozik, *Phys. E* **2002**, *14*, 115–120.
[6] Q. Hao, T. Hegmann, *J. Mater. Chem.* **2006**, *16*, 4197–4205.
[7] Q. K. Liu, Y. X. Cui, D. Gardner, X. Li, S. L. He, I. I. Smalyukh, *Nano Lett.* **2010**, *10*, 1347–1353.
[8] L. J. Martinez-Miranda, K. McCarthy, L. K. Kurihara, *Appl. Phys. Lett.* **2006**, *89*, 161917.
[9] R. Pratibha, W. Park,, I. I. Smalyukh, *J. Appl. Phys.* **2010**, *107*, 063511.
[10] S. Kumar, L. K. Sagari, *Chem. Commun.* **2011**, *47*, 12182–12184.
[11] S. Kumar, V. Lakshminarayanan, *Chem. Commun.* **2004**, 1600–1601.
[12] J. Mirzaei, M. Reznikov, T. Hegmann, *J. Mater. Chem.* **2012**, *22*, 22350–22365.
[13] E. Karatairi, B. Rozic, Z, Kutnjak, V. Tzitzios, G. Nounesis, G. Cordoyiannis, J. Thoen, C. Glorieux, S. Kralj, *Phys. Rev. E* **2010**, *81*, 041703.
[14] G. Cordoyiannis, V. S. R. Jampani, S. Kralj, S. Dhara, V. Tzitzios, G. Nounesis, Z. Kutnjak, C. S. P. Tripathi, P. Losada-Perez, D. Jesenek, C. Glorieux, I. Mušević, A. Zidanšek, H. Ameinitsch, J. Thoen, *Soft Matter* **2013**, *9*, 3956.
[15] L. S. Hirst, J. Kirchhoff, R. Inman, S. Ghosh, Proc. Of SPIE, Conference on Emerging Liquid Crystal Technologies. **2010**, 7618 76180F-1.
[16] A. L. Rodarte, R. Pandolfi, S. Ghosh, L. S. Hirst, *J. Mater. Chem. C* **2013**, *1*, 5527–5532.
[17] I. Mušević, M. Škarabot, U. Tkalec, M. Ravnik, S. Zumer, *Science* **2006**, *313*, 954–958.
[18] Y. D. Gu, N. L. Abbott, *Phys. Rev. Lett.* **2000**, *85*, 4719–4722.
[19] P. Poulin, H. Stark, T. C. Lubensky, D. A. Weitz, *Science* **1997**, *275*, 1770–1773.
[20] U. Tkalec, M. Ravnik, S. Copar, S. Zumer, I. Musevic, *Science* **2011**, *333*, 62–65.
[21] M. Škarabot, I. Mušević, *Soft Matter* **2010**, *6*, 5476–5481.
[22] J. Milette, V. Toader, E. R. Soule, R. B. Lennox, A. D. Rey, L. Reven, *Langmuir* **2013**, *29*, 1258–1263.
[23] J. Milette, S. J. Cowling, V. Toader, C. Lavigne, I. M. Saez, R. B. Lennox, J. W. Goodby, L. Reven, *Soft Matter* **2012**, *8*, 173.
[24] Q. Hao, B. Kinkead, V. M. Marx, H. R. Zhang, T. Hegmann, *ChemPhysChem* **2009**, *10*, 1211–1218.
[25] W. Lewandowski, K. Jatczak, D. Pociecha, J. Mieczkowski, *Langmuir* **2013**, *29*, 3404.
[26] N. Kanayama, O. Tsutsumi, A. Kanazawa, T. Ikeda, *Chem. Commun.* **2001**, 2640–2641.
[27] M. F. Prodanov, N. V. Pogorelova, A. P. Kryshtal, A. S. Klymchenko, Y. Mely, V. P. Semynozhenko, A. I. Krivoshey, Y. A. Reznikov, S. N. Yarmolenko, J. W. Goodby, V. V. Vashchenko, *Langmuir* **2013**, *29*, 9301–9309.
[28] A. L. Rodarte, C. G. L. Ferri, C. Grey, L. S. Hirst, S. Ghosh, Emerging Liquid Crystal Technologies VII: Proc. of SPIE, **2012**, 8279H.
[29] A. L. Rodarte, C. Grey, L. S. Hirst, S. Ghosh, *Phys. Rev. B* **2012**, *85*, 035430.
[30] Y. K. Verma, R. H. Inman, C. G. L. Ferri, H. Mirafzal, S. N. Ghosh, D. F. Kelley, L. S. Hirst, W. C. Chin, S. Ghosh, *Phys. Rev. B* **2010**, *82*, 165428.
[31] A. L. Rodarte, G. Shcherbatyuk, L. Shcherbatyuk, L. S. Hirst, S. Ghosh, *RSC Adv.* **2012**, *2*, 12759–12763.
[32] L. J. Chen, J. D. Lin, S. Y. Huang, T. s. Mo, C. R. Lee, *Adv. Opt. Mater.* **2013**, *1*, 637–643.
[33] K. Kaneko, T. Kawai, N. Nakamura, *ChemPhysChem* **2008**, *9*, 2457–2460.
[34] O. Demmer, A. O. Frank, F. Hagn, M. Schottelius, L. Marinelli, S. Cosconati, R. Brack-Werner, S. Kremb, H.-J. Wester, H. A. Kessler, *Angew. Chem.* **2012**, *124*, 8234–8237; *Angew. Chem. Int. Ed.* **2012**, *51*, 8110–8113.
[35] S. Diez, D. A. Dunmur, M. R. De La Fuente, P. K. Karahaliou, G. Mehl, T. Meyer, M. A. P. Jubindo, D. J. Photinos, *Liq. Cryst.* **2003**, *30*, 1021–1030.
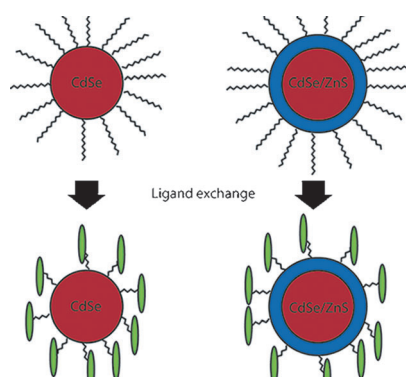
These are not the final page numbers! ↗↗

ARTICLES

A. L. Rodarte, Z. S. Nuno, B. H. Cao,
R. J. Pandolfi, M. T. Quint, S. Ghosh,
J. E. Hein, L. S. Hirst*

■■ – ■■

Tuning Quantum-Dot Organization in Liquid Crystals for Robust Photonic Applications

Dots with liquid-crystalline ligands are synthesized and dispersed in the nematic and cholesteric phases at different concentrations. Fluorescence microscopy, scanning confocal photoluminescence microscopy, and X-ray diffraction reveal details of the quantum-dot (QD) cluster packing. Spectroscopic measurements demonstrate the applicability of the QDs for photonic applications.

These are not the final page numbers! ↗↗